Ore Geology Reviews 125 (2020) 103694

Contents lists available at ScienceDirect

Ore Geology Reviews

journal homepage: www.elsevier.com/locate/oregeorev

Hydrothermal fluid evolution at the Tiegelongnan porphyry-epithermal Cu (Au) deposit, Tibet, China: Constraints from H and O stable isotope and in-situ S isotope

Chao Yang[a,*], Georges Beaudoin[a], Ju-Xing Tang[b], Yang Song[b], Zhi Zhang[c]

[a] Département de géologie et de génie géologique, Université Laval, Québec G1V 0A6, Canada
[b] MLR Key Laboratory of Metallogeny and Mineral Assessment, Institute of Mineral Resources, Chinese Academy of Geological Sciences, Beijing 100037, China
[c] Chengdu Center, China Geological Survey, Chengdu 610081, China

ARTICLE INFO

Keywords:
Muscovite
Alunite
Kaolinite
Stable isotope
SIMS S isotope
Meteoric water
Porphyry

ABSTRACT

The Tiegelongnan porphyry-epithermal Cu (Au) deposit is located in the Duolong porphyry district, north of the Bangong-Nujiang suture zone, Tibet, China. Mineralization is hosted by Jurassic sedimentary sandstone, and several phases of diorite and granodiorite porphyry dikes intruded between 123 and 116 Ma. The hydrothermal alteration is characterized by alunite-kaolinite-dickite overprinting quartz-muscovite-pyrite and biotite alteration zones. Porphyry chalcopyrite-pyrite ± molybdenite (Stage 1) mineralization is associated with biotite alteration. Porphyry chalcopyrite-bornite (Stage 2), and covellite (Stage 3) mineralization is associated with quartz-muscovite-pyrite alteration formed at ~121 Ma. Epithermal mineralization, consisting of pyrite-alunite (Stage 4), chalcopyrite-bornite-digenite (Stage 5), and tennantite-enargite (Stage 6), is hosted by two pulses of alunite-kaolinite breccia and veins at ~116 Ma and ~112 Ma. The fluid composition related to muscovite, with average $\delta^{18}O$ of 8.9‰ and δD of −56‰, indicates a magmatic water origin. Fluid $\delta^{18}O$ composition in equilibrium with quartz veins decreases from 6.7 to 2.3‰, which are likely the results of the water-rock isotopic exchange. Quartz fluid inclusions δD values between −50 to −84‰ are partly lower than that obtained from muscovite alteration fluids, which may result from H fractionation during fluid inclusions decrepitation. Epithermal stage fluid composition equilibrium with alunite yield $\delta^{18}O$ from −1.2 to 2.7‰ and δD from −71 to −51‰, n = 11, which is comparable to the fluid composition equilibrium with Type I kaolinite (hosting ores) with $\delta^{18}O$ between −2.5 and 2.9‰, and δD between −72 and −51‰. It suggests that alunite and Type I kaolinite formed with mixing between magmatic and high altitude Cretaceous meteoric water. Late Types II and III kaolinite (filling alunite and quartz veins) fluid $\delta^{18}O$ and δD values plot along a mixing line between magmatic and low altitude Cretaceous meteoric water, probably following the erosion and plateau subsidence. Porphyry mineralization sulfide stage 1 chalcopyrite and pyrite yield $\delta^{34}S$ values between −5.8 and 0.9‰, with an average fluid $\delta^{34}S_{H2S}$ = −2.5‰ (n = 10), whereas stage 2 chalcopyrite returns $\delta^{34}S$ values from −8.7 to −3‰ with an average $\delta^{34}S_{H2S}$ = −5.6‰ (n = 5). The lower fluid $\delta^{34}S_{H2S}$ values during sulfides stage 2 compared to that of stage 1, suggest that the chalcopyrite-bornite mineralization formed under higher oxidation conditions than that of the chalcopyrite-pyrite mineralization. Alunite yields $\delta^{34}S$ values from 11 to 18.3‰ (n = 8), and the associated sulfide stage 4 pyrite have varying $\delta^{34}S$ values from −32.2 to 5.4‰. Disequilibrium S isotope in alunite-pyrite pairs was likely because of rapid cooling and retrograde S isotope exchange during later sulfides emplacement. Epithermal mineralization sulfide Stage 4 S-equilibrated pyrite (−14.9 to −9.5‰), Stage 5 chalcopyrite (−11.6 to −8.2‰), and Stage 6 enargite (−5.4 to −2.6‰) display increasing $\delta^{34}S$ values suggesting epithermal fluid compositions evolve towards more reducing conditions.

1. Introduction

Porphyry hydrothermal system is widely recognized derived from magmatic fluids, however, exotic fluids, such as seawater and meteoric water, are also involved in the formation and reconstruction of this system (Dilles et al., 1992; Seedorff et al., 2005; Orovan et al., 2018). Meteoric water is the most common exotic fluids in porphyry-related system, which is principally involved with the formation of alunite-

* Corresponding author.
E-mail address: chaoyangcn8@gmail.com (C. Yang).

https://doi.org/10.1016/j.oregeorev.2020.103694
Received 20 March 2020; Received in revised form 14 July 2020; Accepted 22 July 2020
Available online 27 July 2020
0169-1368/

kaolinite alteration at the top of porphyry hydrothermal system (Stoffregen, 1987; Hedenquist and Taran, 2013). It also contributes to the reconstructions of the porphyry hydrothermal system, such as cooling and overprinting of porphyry hydrothermal alterations (Sheppard and Taylor, 1974; Gustafson and Hunt, 1975), supergene oxidization and enrichment (Sillitoe, 2005), and exhumation of the porphyry-related system (Yanites and Kesler, 2015). Alunite is one of the key minerals for exploring and understanding the hydrothermal environment of epithermal deposits (Rye, 1993; Deyell et al., 2005; Chang et al., 2011). Alunite commonly forms as a result of magmatic vapor condensing in groundwater, causing a pH decrease in the epithermal environment (Stoffregen, 1987; Hedenquist and Taran, 2013). Alunite and associated sulfides S isotope compositions offer information about the hydrothermal fluid temperature and redox state of the system (Rye et al., 1992; Stoffregen et al., 1994). However, alunite can also form under other different conditions during magmatic steam, steam heated, and supergene alteration, showing varying O, H, and S stable isotope signatures (Rye et al., 1992; Rye, 1993), which should be discriminated in exploration for epithermal deposits.

The Tiegelongnan deposit, located in the Duolong district, north of the Bangong-Nujiang suture zone, Tibet, China, is a large porphyry-epithermal deposit containing measured, indicated, and inferred resources of 2089 Mt grading 0.53% Cu (Jinlong Mining Co., Ltd, 2017). The gold grade is low at 0.08 g/t (Tang et al., 2017). Tiegelongnan was the first porphyry Cu (Au) deposits with high-sulfidation epithermal alteration and mineralizations discovered in Tibet (Tang et al., 2014). It formed with multiple phases of Cretaceous high-K calc-alkaline intermediate and felsic porphyritic intrusions. The primary porphyry mineralization took place at ~120 Ma associated with porphyry stage biotite and quartz-muscovite-pyrite alteration, which is overprinted by two main epithermal mineralization pulses with alunite-kaolinite-dickite alteration at ~116 Ma and ~112 Ma (Lin et al., 2017a; Yang et al., 2020). Supergene oxidation and enrichment are present at the shallow level of the deposit. Exhumation of this deposit started after its initial formation and continued till now. The compositions of the hydrothermal fluids that formed alteration and mineralization of the Tiegelongnan deposit, however, remains mostly unknown.

Although, a small amount of quartz O and fluid inclusions H stable isotopes (n = 8) indicate a magmatic fluid origin at Tiegelongnan (Lin et al., 2017b), no porphyry stage hydrothermal aluminosilicate or epithermal stage alteration mineral has been investigated for their stable isotope compositions. Lin et al. (2017b) and Wang et al. (2017) presented sulfides and gypsum bulk mineral S isotope compositions, and proposed a mantle S source. However, the S isotope compositions in relation with sulfide paragenetic sequence, S isotope equilibrium conditions between sulfide and sulfate, and redox state evolution of hydrothermal fluids were not discussed. Therefore, the objective of this paper is to investigate H, O, and S (including in situ S analyses) isotopes of hydrothermal minerals based on detailed evolution of the hydrothermal system with paragenetic sequence, and to discuss the composition of the hydrothermal fluids, and metals precipitation environment, during the evolution of porphyry and epithermal hydrothermal events in the Tiegelongnan deposit.

2. Geology

2.1. Duolong district

The Duolong district is a large porphyry-epithermal Cu-Au system, located in the western Bangong-Nujiang Suture Zone, mid-west Tibet, China (Fig. 1a and b). This porphyry-related system is hosted by a continental arc, related to the Cretaceous northward subduction of the Bangong-Nujiang Ocean plate under the Southern Qiangtang terrane (Zhu et al., 2016). The Duolong district consists of several porphyry and epithermal deposits and prospects (Fig. 1c). Duobuza and Bolong were the first two porphyry Au-Cu deposits discovered in the district (Li et al., 2013). The Naruo porphyry Cu-Au deposit and Tiegelongnan porphyry-epithermal Cu (Au-Ag) deposit were discovered in 2013 (Tang et al., 2014; Ding et al., 2017; Lin et al., 2018). The Nadun deposit is recognized as a high-sulfidation epithermal Cu-Au deposit (Li et al., 2016a). Gaerqin is an epithermal Cu-Au mineralization prospect, whereas Dibao, Sena, and Saijiao are porphyry Cu-Au mineralization prospects.

The oldest sedimentary rocks in the Duolong district are the Upper Triassic Riganpeicuo Formation limestones (Fig. 1c), overlain by Upper to Middle Jurassic Sewa and Quse formations sandstone, siltstone, and claystone, which hosts the porphyry deposits. The Cretaceous Meiriqiecuo Formation consists of basalt, andesite, dacite, rhyolite, and pyroclastic rocks that unconformably overlies the Sewa and Quse formations. The Oligocene Kangtuo Formation conglomerate unconformably overlies the Jurassic sedimentary and Cretaceous volcanic rocks. Quaternary eluvial sediments cover the north-western and south-eastern parts of the Duolong area.

Dozens of Cretaceous intrusive dikes are present in the Duolong district (Fig. 1c). Most intrusions are intermediate to felsic porphyry rocks, including diorite, quartz diorite, and granodiorite, which are associated with the formation of the porphyry and epithermal deposits (Li et al., 2014; Sun et al., 2017). These intrusions were emplaced between 126 and 116 Ma, whereas post-mineral volcanic rocks of the Meiriqiecuo Formation erupted between 114 and 105 Ma (Wang et al., 2015; Li et al., 2016b; Li et al., 2017; Lin et al., 2017a).

2.2. Tiegelongnan deposit

The Tiegelongnan deposit is hosted by the Jurassic Sewa Formation sandstone, which is unconformably covered by Cretaceous andesite and Oligocene Kangtuo Formation conglomerate (Fig. 1d). Several pulses of porphyry dikes were emplaced in Jurassic sandstone between ~123 and ~116 Ma (Fang et al., 2015; Lin et al., 2017b; Zhang et al., 2018; Yang et al., 2020). Several deep boreholes encountered biotite hornfels below 4100 m elevation (Fig. 2a). The Cretaceous Meiriqiecuo Formation andesite covers the top of the Tiegelongnan deposit, along an angular unconformity over a layer of erosional breccia on the top of the Jurassic Quse Formation sandstone (Fig. 2a). The western and southern parts of the andesite are overlain by piedmont and steam gravel (Fig. 2a) that conceal the hydrothermal mineralization and alteration, and porphyritic intrusions. The Rongna NW-striking reverse fault dips steeply to the south, and displaces andesite and ore in the southern part of this deposit (Song et al., 2018).

3. Alteration and mineralization

The main hydrothermal alteration stages, and their associated hydrothermal mineralogy and sulfides stage are summarized in Fig. 3. Biotite, quartz-muscovite-pyrite, and chlorite alterations are associated with porphyry sulfide mineralization, whereas alunite-kaolinite-dickite alteration host the epithermal sulfide mineralization.

3.1. Biotite alteration

A small volume of biotite alteration is present at depth (Fig. 2b), characterized by hydrothermal biotite-chalcopyrite (EB) vein, and hydrothermal biotite in quartz-molybdenite-chalcopyrite-pyrite (B1-type) veins. The vein-hosted hydrothermal biotite differs from the disseminated metamorphic biotite in the hornfels. Hydrothermal biotite at Tiegelongnan is Mg-rich, whereas metamorphic biotite is Fe-rich (Yang, unpublished data). Hydrothermal biotite fills in the center of quartz veins, and it is replaced by kaolinite (Fig. 4a). Biotite alteration is overprinted by muscovite-quartz-pyrite alteration (Fig. 3). One hydrothermal biotite yielded a ^{40}Ar-^{39}Ar age of 121.1 ± 0.6 Ma (Lin et al., 2017a). Disseminated chalcopyrite and pyrite, and B1 vein-hosted chalcopyrite, pyrite, and molybdenite are Stage 1 sulfides

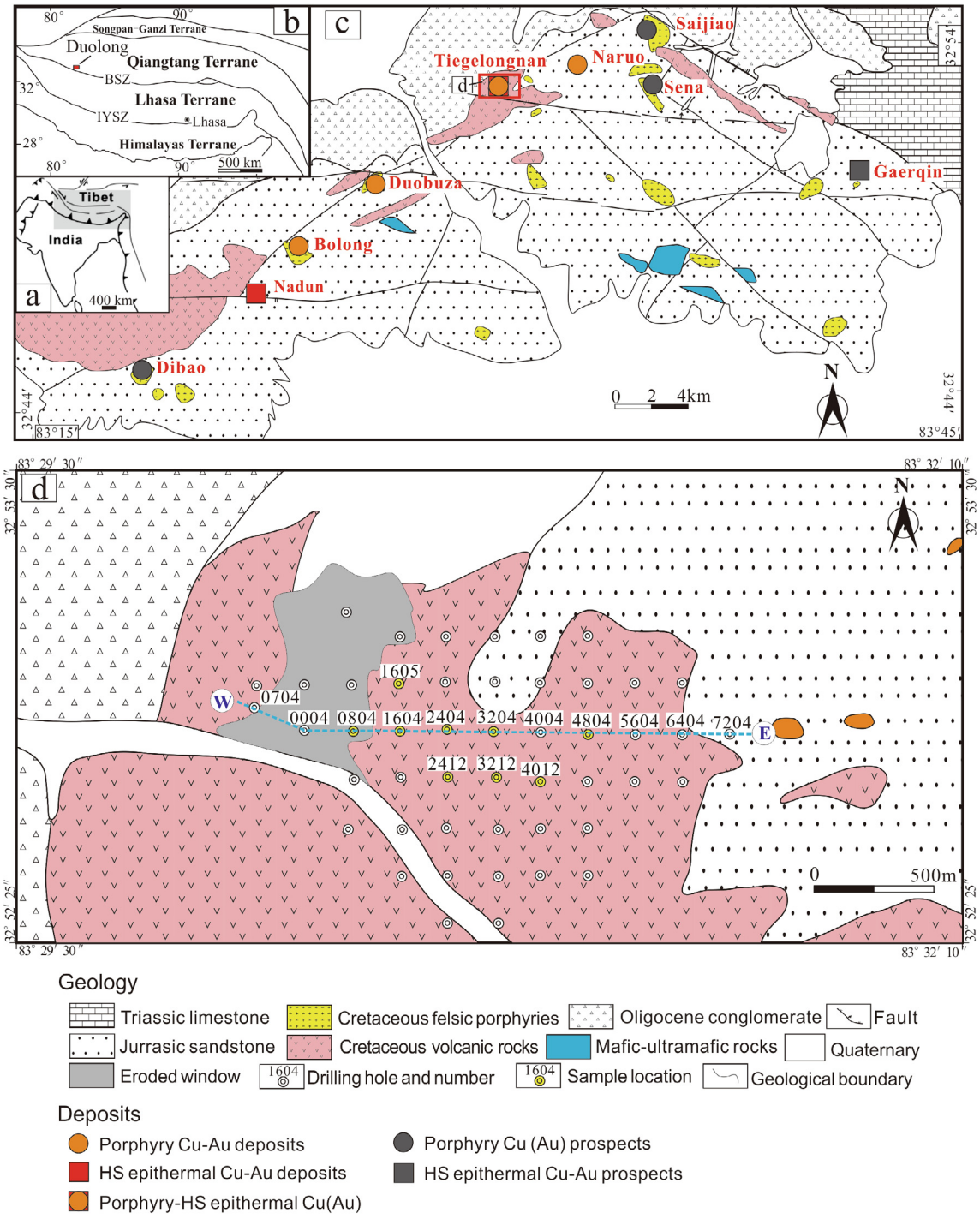

Fig. 1. a, b) Location of the study area; c) Geology of the Duolong porphyry Cu-Au district; d) Geology and sample location of the Tiegelongnan deposit.

mineralization present in the biotite alteration zone (Fig. 3).

3.2. Chlorite alteration

Chlorite alteration is present at the eastern periphery of Tiegelongnan (Fig. 2b), characterized by an assemblage of chlorite-pyrite ± epidote ± calcite ± illite. Chlorite-pyrite, a few pyrite-quartz (D-type) vein, and pyrite veins occur in this zone. Pyrite ± chlorite veins are also named as C veins by Zhang et al. (2018). Mineralization occurs as minor chalcopyrite-pyrite and supergene chalcocite veins.

3.3. Quartz-muscovite-pyrite alteration

A large part of granodiorite porphyry intrusions and sandstone wall rocks are affected by quartz-muscovite-pyrite alteration. Feldspar phenocrysts and the matrix of granodiorite porphyries are mostly altered to muscovite. Muscovite was dated by ^{40}Ar-^{39}Ar at the age of 120.9 ± 0.8 Ma, which is similar to the ages of main ore-bearing porphyries and hydrothermal biotite, although a younger muscovite age of 108.7 ± 0.7 Ma obtained (Yang et al., 2020). A-type quartz-chalcopyrite-borntie vein is cut by B2-type quartz-molybdenite veins (Fig. 4b) at depth (> ~800 m) in the quartz-muscovite-pyrite alteration zone. D-type quartz-pyrite and pyrite veins are commonly present in

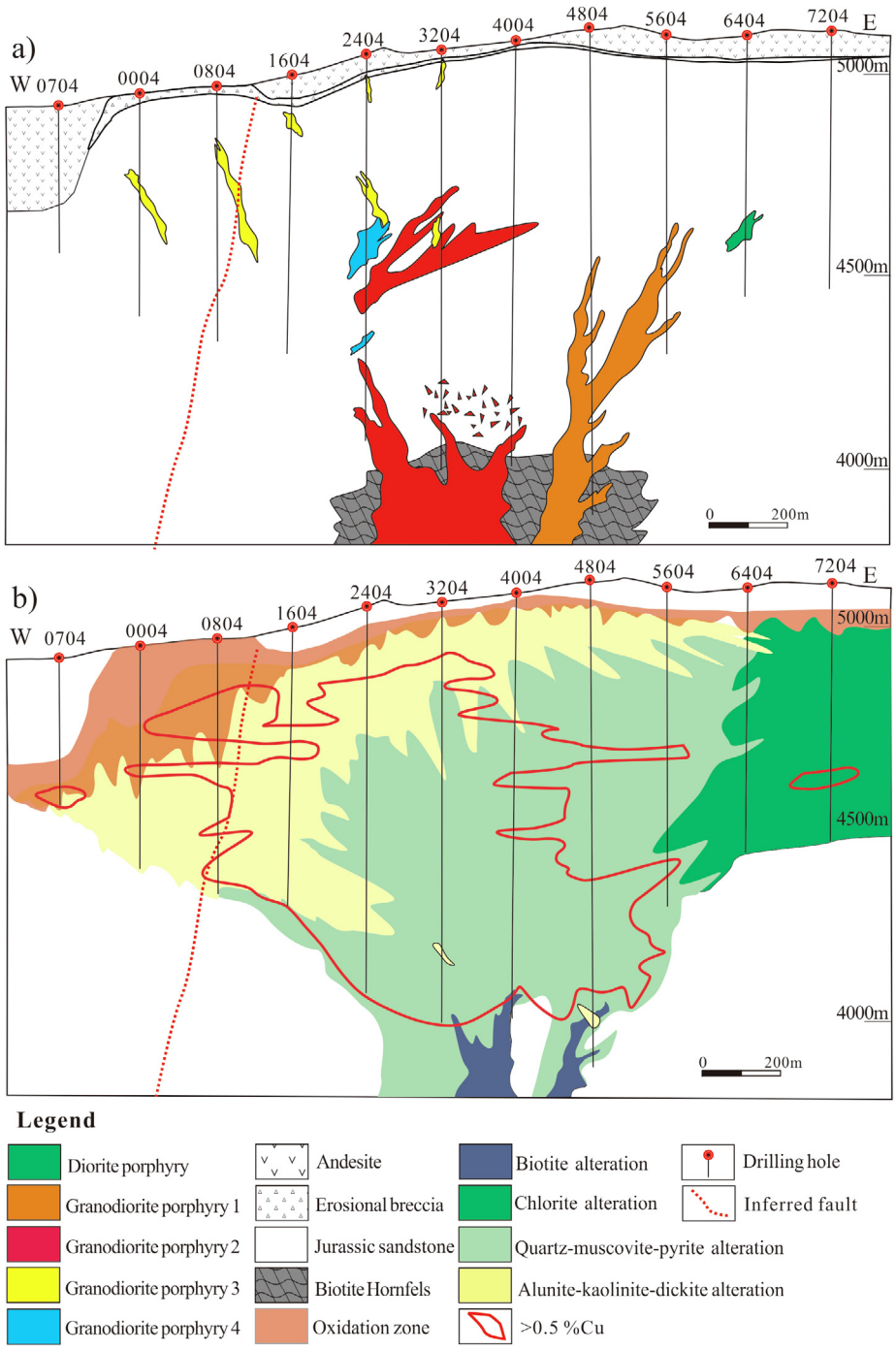

Fig. 2. a) Geology, and b) hydrothermal alteration of the W-S cross-section of Tiegelongnan.

this alteration and cut A and B2 veins (Fig. 4c). Trace amounts of anhydrite occur in A veins, whereas gypsum is present in A and D veins. Rutile is widespread in all types of quartz veins and as disseminated grains in the altered sandstones and porphyry dikes. Pyrophyllite is found at upper parts of this alteration zone. Stage 2 chalcopyrite and bornite, as extensive disseminated and minor in A vein, cement and replace pyrite (Fig. 4d), associated with quartz-muscovite-pyrite alteration. Some chalcopyrite and bornite are replaced by Stage 3 covellite (Fig. 4e) above the 4500 m elevation.

3.4. Alunite-kaolinite-dickite alteration

Alunite-kaolinite-dickite (advanced argillic) alteration is present in the shallow part of the deposit above 4700 m elevation but deepens to 4300 m elevation in the western part of the deposit (Fig. 2b). Alunite and kaolinite are the dominant minerals, whereas dickite and pyrophyllite are present only in the deep portion of the alteration zone, and in the periphery of quartz-muscovite-pyrite alteration. The alunite-kaolinite-dickite alteration overprints quartz-muscovite-pyrite, chlorite alteration, and biotite alteration, characterized by kaolinite- and alunite-bearing veins cutting A, C and D veins, and by kaolinite and alunite filling in earlier A, B, C, D, and pyrite veins, and by replacement of biotite and muscovite by kaolinite (Lin et al., 2017a; Zhang et al., 2018; Yang et al., 2020).

Several types of alunite are recognized from hydrothermal breccia and alunite veins. Type I alunite occurs with pyrite, enargite, and

	Hydrothermal stages	^{40}Ar-^{39}Ar Ages (Ma)	Alteration mineralogy	Sulfide paragenesis	Overprinting relationship
Epithermal	Alunite-kaolinite-dickite-pyrophyllite	Alunite 116.3±0.8 & 111.7±1.0[1]	Alunite, kaolinite, dickite, ±pyrophyllite, ±quartz, ±rutile, ±goyazite, ± diaspore, ±nacrite	S6:enargite-tennantite, S5:bornite-chalcopyrite ±digenite, S4: pyrite-alunite	
Porphyry	Quartz-muscovite -pyrite	Muscovite 120.9±0.8[1]	Quartz, muscovite, ±phlengite, ±magnetite, ±anhydrite, ±rutile, ±hematite, ±tourmaline	S3: covellite S2: chalcopyrite-bornite	
	Chlorite		Chlorite, epidote, calcite, ±hematite	Pyrite±chalcopyrite	
	Biotite	Biotite 121.1±0.6[2]	Biotite, ±magnetite, ±rutile	S1: chalopyrite-pyrite ±molybdenite	

Fig. 3. Hydrothermal alteration and mineralization stages in the Tiegelongnan deposit. ^{40}Ar-^{39}Ar data of 1 from Yang et al., (2020), and 2 from Lin et al., (2017a).

tennantite cementing quartz-muscovite-pyrite-altered clasts in hydrothermal breccia (Fig. 4f). Pyrite is usually replaced by enargite and tennantite. Type II alunite is widespread as laminated alunite-sulfide veins, which is associated with the main epithermal mineralization stage of pyrite, bornite, chalcopyrite, digenite, enargite, and tennantite mineralization. Minor pyrophyllite was found in this type of alunite veins (Zhang et al., 2018). Pyrite, with alunite, represents the Stage 4 sulfides, followed by the replacement of the Stage 5 chalcopyrite-bornite-digenite. The Stage 6 Enargite and tennantite replace chalcopyrite-bornite-digenite, and earlier pyrite (Fig. 4g). Enargite commonly forms exsolution of or is replaced by tennantite. Type III alunite fills D vein, without pyrite. Type IV alunite forms wide alunite-pyrite veins. These alunite returned ^{40}Ar-^{39}Ar ages of 116.3 ± 0.8 Ma for type I, 111.7 ± 1.0 Ma for type II, 112.5 ± 0.8 Ma for type III, and ~100.6 ± 2.0 Ma for type IV (Yang et al., 2020).

Three types of kaolinite are discriminated in this study. Type I

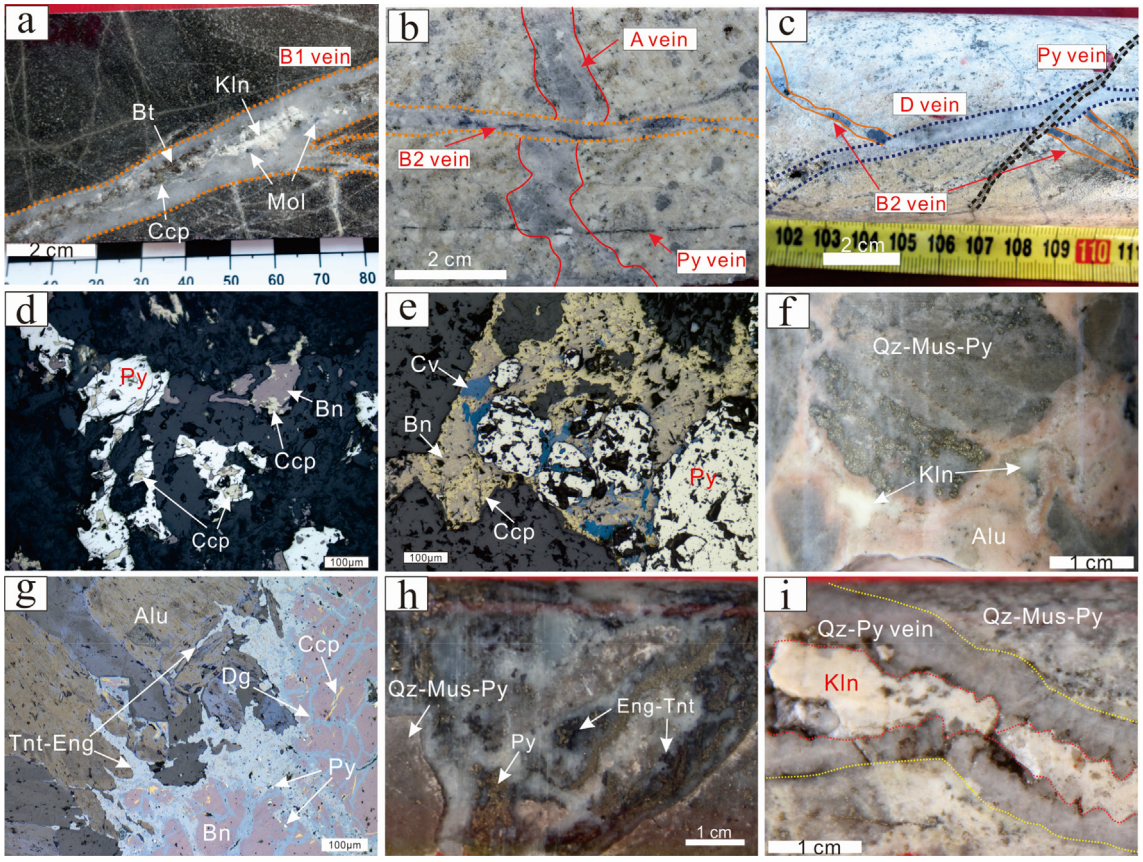

Fig. 4. Overprinting relationship of different alteration, vein, and sulfide stages. a) Biotite in quartz-chalcopyrite-pyrite-molybdenite (B1) vein, and replaced by Type II kaolinite; b) quartz-chalcopyrite-bornite (A) vein cut by quartz-molybdenite (B2) and pyrite veins; c); B2 vein cut by quartz-pyrite (D) vein, and by pyrite vein; d) Disseminated chalcopyrite-bornite filling voids in pyrite; e) chalcopyrite-bornite replaced by covellite; f)- Quartz-muscovite-pyrite breccia in alunite, and Type III late barren kaolinite filling alunite; g)- Pyrite in alunite veins is replaced by chalcopyrite-bornite-digenite, which is replaced by younger enargite-tennantite; h)- Early Type I kaolinite-pyrite-enargite-tennantite vein cuts quartz-muscovite-pyrite altered host rock; i)- Late Type II barren kaolinite vein filling reopening of D-type quartz-pyrite vein. Alu-alunite, Bn-bornite, Bt-biotite, Dg-digenite, Ccp-chalcopyrite, Cv-covellite, Eng-enargite, Kln-kaolinite, Mus-muscovite, Py-pyrite, Qz-quartz, Tnt-tennantite.

Table 1
Hydrogen and Oxygen isotope data and calculated fluid composition.

Sample No.	Sample description	Calculate T (°C)	Mineral	Data		Fluid		^{40}Ar-^{39}Ar Ages (Ma)[1]
				$\delta^{18}O$ (VSMOW ‰)	δD (VSMOW ‰)	$\delta^{18}O_{H2O}$ (VSMOW ‰)	δD_{H2O} (VSMOW ‰)	
Biotite alteration								
4804–1224	Qz-Mol-Ccp-Py-Bio vein	400	Biotite	12.6	−75	14.7	−25	
			Quartz	8.3	−35	4.2	−35	
4804–1245	Qz-Mol-Py vein	400	Quartz	10.5	−64	6.4	−64	
4804–1234	Qz-Mol-Bio vein	400	Quartz	8.9	−62	4.8	−62	
4804–1203	Qz-Mol-Py vein	400	Quartz	9.3	−59	5.2	−59	
Qz-Mus-Py alteration								
4804–1152	Sericite altered G1 porphyry	350	Muscovite	12.6	−81	10.4	−61	
2404–737	Sericite altered G2 porphyry	350	Muscovite	7.0	−75	4.8	−55	120.9 ± 0.8
4804–1203	Sericite halos around Qz-Mol vein	350	Muscovite	11.1	−72	8.9	−52	
1604–117	Sericite altered G3 porphyry	350	Muscovite	13.7	−82	11.5	−62	
2404–313	Mus altered G3 porphyry	350	Muscovite	7.0	−72	4.8	−52	108.7 ± 0.7
4012–1010	Qz-Py-Ccp-Bn vein	350	Quartz	10.7	−57	5.4	−57	
4804–1223	Qz-Ccp-Py vein with filling of Kln	350	Quartz	11.2	−73	5.9	−73	
2404–903	Qz-Py-Ccp-Bn vein	350	Quartz	7.9	−83	2.6	−83	
2404–840	Qz-Py-Ccp-Bn vein replaced by Tnt	350	Quartz	7.6	−61	2.3	−61	
3212–723	Qz-Py-Ccp-Bn vein	350	Quartz	9.7	−71	4.4	−71	
1604–650	Qz-Py-Ccp vein replaced by Cv	350	Quartz	11.4	−66	6.1	−66	
2404–536	Qz-Py-Ccp vein replaced by Cv	350	Quartz	9.2	−79	3.9	−79	
2412–511	Qz-Py vein with filling of Alu	320	Quartz	10.7	−50	4.5	−50	
2404–374	Qz-Py vein replaced by Dg, with filling of Kln	320	Quartz	10.4	−81	4.2	−81	
2404–412	Qz-Py vein replaced by Dg and Bn	320	Quartz	8.8	—	2.6	—	
2405–227	Qz-Py vein replaced by Dg	320	Quartz	12.9	−64	6.7	−64	
1604–156	Qz-Py vein	320	Quartz	10.2	−70	4.0	−70	
2405–206	Qz vein with filling of Kln	320	Quartz	9.4	−84	3.2	−84	
Alunite								
1604–429	Alu-Sul vein cemented hydrothermal breccia	250	AluniteI	8.9	−68	0.6	−60	116.3 ± 0.8
1604–171	Laminated Alu-Sul vein	250	AluniteII	10.9	−72	2.6	−64	111.7 ± 1.0
1604–149	Laminated Alu-Sul vein	250	AluniteII	10.5	−74	2.2	−66	
1604–375	Alu-Sul-Kln vein in Py vein	250	AluniteII	10.3	−67	2.0	−59	
4012–354	Alu-Gn-Sp vein	250	AluniteII	7.1	−79	−1.2	−71	
1604–231	Laminated Alu-Sul	250	AluniteII	–	−76	–	−68	
0804–408	Laminated Alu-Sul	250	AluniteII	9.1	−69	0.8	−61	
0804–563	Laminated Alu-Sul	250	AluniteII	8.5	−69	0.2	−61	
2412–511	Alu filling in Qz-Py vein	250	AluniteIII	11.0	−59	2.7	−51	112.5 ± 0.8
3212–206	Alu-Sul vein with Kln-Py clasts	250	AluniteIV	10.1	−73	1.8	−65	100.6 ± 2.0
Kalinite								
2404–269	Kln-Sul vein	100	KaoliniteI	5.9	−96	−7.2	−72	
0804–317	Kln-Hem-Sul vein	100	KaoliniteI	14.3	−74	1.2	−51	
2404–276	Kln vein cutting Py vein	100	KaoliniteI	10.6	−96	−2.5	−72	
2405–471	Kln-Sul vein	100	KaoliniteI	3.4	−77	−9.7	−53	
2405–567	Kln-Sul vein	100	KaoliniteI	11.3	−85	−1.8	−61	
2412–282	Kln-Sul vein	100	KaoliniteI	13.4	−90	0.3	−66	
2404–92	Kln-Hem vein	100	KaoliniteI	12.9	−81	−0.2	−58	
2405–206	Kln-Hem filling in Qz vein	100	KaoliniteI	12.2	−93	−0.9	−69	
4804–1223	Barren Kln filling in Qz vein	100	KaoliniteII	16.0	−70	2.9	−47	
2412–407	Barren Kln filling in Qz vein	100	KaoliniteII	10.9	−65	−2.2	−42	
1604–429	Barren Kln filling in Alu-Sul vein	100	KaoliniteIII	7.1	−66	−6.0	−43	
1604–231	Barren Kln in Alu-Sul vein	100	KaoliniteIII	15.1	−65	2.0	−41	

1-^{40}Ar-^{39}Ar ages from Yang et al., (2020)
δD_{H2O} of fluid composition from quartz is from the fluid inclusions from mechanical decrepitation.
Alu-alunite, Bio-biotite, Bn-bornite, Ccp-chalcopyrite, Cv-covellite, Dic-dickite, Dg-digenite, Hem-hematite, Gp-galena, Mol-molybdenite, Mus-muscovite, Kln-kaolinite, Py-pyrite, Qz-quartz, Sp-spalerite, Sul-sulfide, Tnt-tennantite.

kaolinite veins occur with pyrite, enargite, and tennantite (Fig. 4h), and with hematite locally. Late type II kaolinite fills in earlier quartz veins (Fig. 4i). Type III kaolinite fills type I and II alunite veins (Fig. 4f) in the shallow part. Types II and III kaolinite usually occur without sulfides or oxides, as late stage products.

3.5. Supergene zone

Supergene oxidation at the top of the hydrothermal alteration system (Fig. 2b) is characterized by the occurrence of jarosite, limonite, goethite, hematite, Cu-oxides, and kaolinite. Part of the chlorite and alunite-kaolinite-dickite alteration zones are affected by the supergene oxidation. Sulfides in alunite-sulfide veins and kaolinite-sulfide veins are oxidized to hematite and Cu-oxides.

4. Analytical methods

Representative core samples are collected from the W-S cross-section and several other drilling holes (Fig. 1d). Biotite (n = 1), muscovite (n = 5), quartz (n = 13), alunite (n = 10), and kaolinite (n = 12) were separated for O and H isotope analysis, alunite (n = 10), pyrite (n = 5), and enargite (n = 4) for bulk mineral S isotope analysis. Eight polished thin-sections are prepared for pyrite (n = 16) and chalcopyrite (n = 10) in situ S isotope analysis. The O, H, and bulk mineral S

isotopes were analyzed at the Queen's Facility for Isotope Research in Queen's University, Canada. Oxygen in silicates was extracted from 5 mg samples at 550–600 °C according to the conventional BrF5 procedure of (Clayton and Mayeda, 1963) and analyzed via a dual inlet on a Thermo-Finnigan DeltaPlus XP Isotope-Ratio Mass Spectrometer (IRMS). Alunite samples are dissolved in 2 N HCl and re-precipitated as $BaSO_4$ using a saturated solution of $BaCl_2$ for O isotope analysis. The oxygen isotopic composition was measured using a MAT 253 Stable Isotope Ratio Mass Spectrometer coupled to a Thermo Scientific TC/EA High-Temperature Conversion Elemental Analyzer. Biotite, muscovite, alunite, and kaolinite samples for hydrogen isotope analysis were weighed into silver capsules, degassed for 1 h at 100 °C then crushed and loaded into a zero-blank autosampler. The hydrogen of quartz is extracted from fluid inclusions with mechanical decrepitation. The hydrogen isotopic composition was measured using a Thermo-Finnigan thermo-combustion elemental analyzer (TC/EA) coupled to a Thermo-Finnigan DeltaPlus XP Continuous-Flow IsotopeRatio Mass Spectrometer (CF-IRMS). $\delta^{18}O$ and δD values are reported using the delta (δ) notation in ‰ (‰) relative to Vienna Standard Mean Ocean Water (VSMOW), with a precision of 0.1‰ and 3‰ respectively.

Alunite S isotope was analyzed from precipitates of barite, using a saturated solution of $BaCl_2$ to avoid contamination from sulfide. Sulfur isotopic composition was measured using a MAT 253 Stable Isotope Ratio Mass Spectrometer coupled to a Costech ECS 4010 Elemental Analyzer. The $\delta^{34}S$ values are reported relative to Vienna Canyon Diablo Troilite (VCDT), with a precision of 0.2‰.

The Cameca IMS 4f Secondary Ion Mass Spectrometer at the MAF-IIC Microanalysis Facility of Memorial University was used for in situ pyrite and chalcopyrite S isotope analysis. The $\delta^{34}S$ determinations were performed using a primary Cs ion beam of 0.6–0.8 nA, accelerated through a 10 keV potential, and focused into a 5–15 μm diameter spot. To exclude exotic material in the polished surface from analysis, each spot was first pre-sputtered for 120 s with a 25 μm square raster applied to the beam then pre-sputtered again using a 10 μm raster for 200 s. All peak signals were collected with an ETP 133H multiple-dynode electron multiplier and processed through ECL-based pulse-counting electronics with an overall dead time of 11 ns. Background measurements at the nominal mass 31.67 Da were taken during each magnetic switching cycle - and were routinely less than 0.05–0.1 counts per second. Count rates on ^{32}S were maintained between 1,000,000 and less than 1,500,000 counts per second by adjusting the primary beam current for each sulfide phase. Overall reproducibility, based on replicate standard analyses, is typically better than ± 0.35–0.45‰ (1σ).

5. Results

5.1. Oxygen and hydrogen isotopes

Oxygen and hydrogen isotope data of gangue minerals and their associated fluid composition are given in Table 1 and Fig. 5. Fluid composition calculation equations are given in Table 3. The temperature used for fluid composition calculation for biotite, muscovite, and quartz is based on fluid inclusion study of Yang et al. (2014) and He et al. (2017), which indicated that biotite and B1 veins formed at a temperature of ~400 °C, A vein and muscovite alteration formed at ~350 °C, D vein formed at ~320 °C. Calculation temperature for alunite is 250 °C and that for kaolinite is 100 °C, based on the mineral stability temperatures of alunite and kaolinite estimated by Stoffregen (1987) and Watanabe and Hedenquist (2001).

5.1.1. Biotite

One hydrothermal biotite from a quartz-molybdenite-biotite vein gives $\delta^{18}O$ and δD values of 12.6‰ and −75‰ (Fig. 5a). Assuming an average temperature of 400 °C, the calculated $\delta^{18}O_{H2O}$ in equilibrium with the biotite is 14.7‰, using the fractionation of Zheng (1993b), and that of δD_{H2O} is −25‰(Fig. 5b), using the fractionation of Suzuoki and Epstein (1976).

5.1.2. Muscovite

Four muscovite samples from quartz-muscovite-pyrite alteration give $\delta^{18}O$ values from 7.0 to 13.7‰, and δD values from −82 to −72‰, respectively (Fig. 5a). Hydrothermal fluid compositions in equilibrium with muscovite were calculated using the O fractionation of O'Neil and Taylor (1969) and the H fractionation of (Marumo et al. (1980)), and a fluid inclusion homogenization temperature of 350 °C. The fluid compositions $\delta^{18}O_{H2O}$ are between 4.8 and 11.5‰, with an average value of 8.9‰, and δD_{H2O} compositions are between −62 and −52‰ with an average value of −58‰ (Fig. 5b).

The younger (~109 Ma) muscovite sample from the shallow portion of quartz-muscovite-pyrite alteration gives $\delta^{18}O$ value of 7.0‰, and δD value of −72‰ (Fig. 5a). The fluid compositions in equilibrium with muscovite at a temperature of 350 °C are $\delta^{18}O_{H2O}$ of 4.8‰, and δD_{H2O} of –52‰ (Fig. 5b).

5.1.3. Quartz from B1-veins in biotite alteration

The measured $\delta^{18}O$ values of four quartz samples from quartz-molybdentie- ± chalcopyrite ± pyrite ± biotite (B1) type veins are between 8.3 and 10.5‰, with δD values of fluid inclusion water between −64 and −35‰. Fluid O isotope compositions in equilibrium with quartz are calculated using fractionation of Zheng (1993a), with $\delta^{18}O_{H2O}$ values from 4.2 and 6.4‰ at a temperature of 400 °C. One quartz sample with biotite has a $\delta^{18}O$ value of 8.3‰, and the calculated $\delta^{18}O_{H2O}$ value of water in equilibrium with the quartz is 6.1‰, in contrast to the biotite water $\delta^{18}O_{H2O}$ value of 14.7‰, which indicate quartz and biotite are not in O isotope equilibrium. Fluid inclusions from these quartz give $\delta^{18}D_{H2O}$ from −64 to −35‰.

5.1.4. Quartz from A-veins in sericite alteration

Eight quartz samples from quartz-chalcopyrite-pyrite ± bornite (A) veins yield $\delta^{18}O$ values from 7.6 to 11.4‰ and fluid inclusion δD values from −83 to −50‰. Calculated water compositions in equilibrium with quartz are $\delta^{18}O_{H2O}$ from 2.3 to 6.1‰, at a temperature of 350 °C.

5.1.5. Quartz from D-veins in sericite alteration

Five quartz samples from quartz-pyrite (D) vein give $\delta^{18}O$ values from 8.8 to 12.9‰, four of them have fluid inclusion δD values from −84 to −64‰. Calculated water compositions $\delta^{18}O_{H2O}$ associated with quartz are between 2.6 and 6.7‰, at a temperature of 320 °C.

5.1.6. Alunite

Type I alunite breccia gives $\delta^{18}O$ and δD values of 8.9 and −68‰. Seven Type II alunite have $\delta^{18}O$ values ranging from 7.1 to 10.9‰, and δD values from −79 to −67‰. One Type III alunite sample gives $\delta^{18}O$ and δD values of 11.0 and −59‰. One Type IV alunite sample gives $\delta^{18}O$ and δD values of 10.1 and −73‰. Fluid compositions of all stages of alunite are similar, with $\delta^{18}O_{H2O}$ values from −1.2 to 2.7‰ (mean = 1.2, n = 9), and δD_{H2O} values from −71 to −51‰ (mean = -62, n = 10; Table 1, Fig. 5b), which are calculated at 250 °C using the fractionation of Stoffregen et al. (1994).

5.1.7. Kaolinite

Eight Type I kaolinite vein samples yield variable $\delta^{18}O$ values between 3.4 and 14.3‰, and δD values between −96 and −74‰. The fluid in equilibrium with the kaolinite at a temperature of 100 °C has $\delta^{18}O_{H2O}$ values from −7.2 and 1.2‰, and δD_{H2O} values from −72 and −51‰, using the fractionation of Sheppard and Gilg (1996). Two Type II kaolinite samples filling quartz veins give $\delta^{18}O$ values of 10.9 and 16.0‰, and δD values of −75 and −65‰. Fluid compositions in equilibrium with these kaolinite filling quartz veins have $\delta^{18}O_{H2O}$ values of −2.2 and 2.9‰, and δD_{H2O} values from −47 to −42‰ (Fig. 5b). Two Type III kaolinite samples filling alunite veins give $\delta^{18}O$

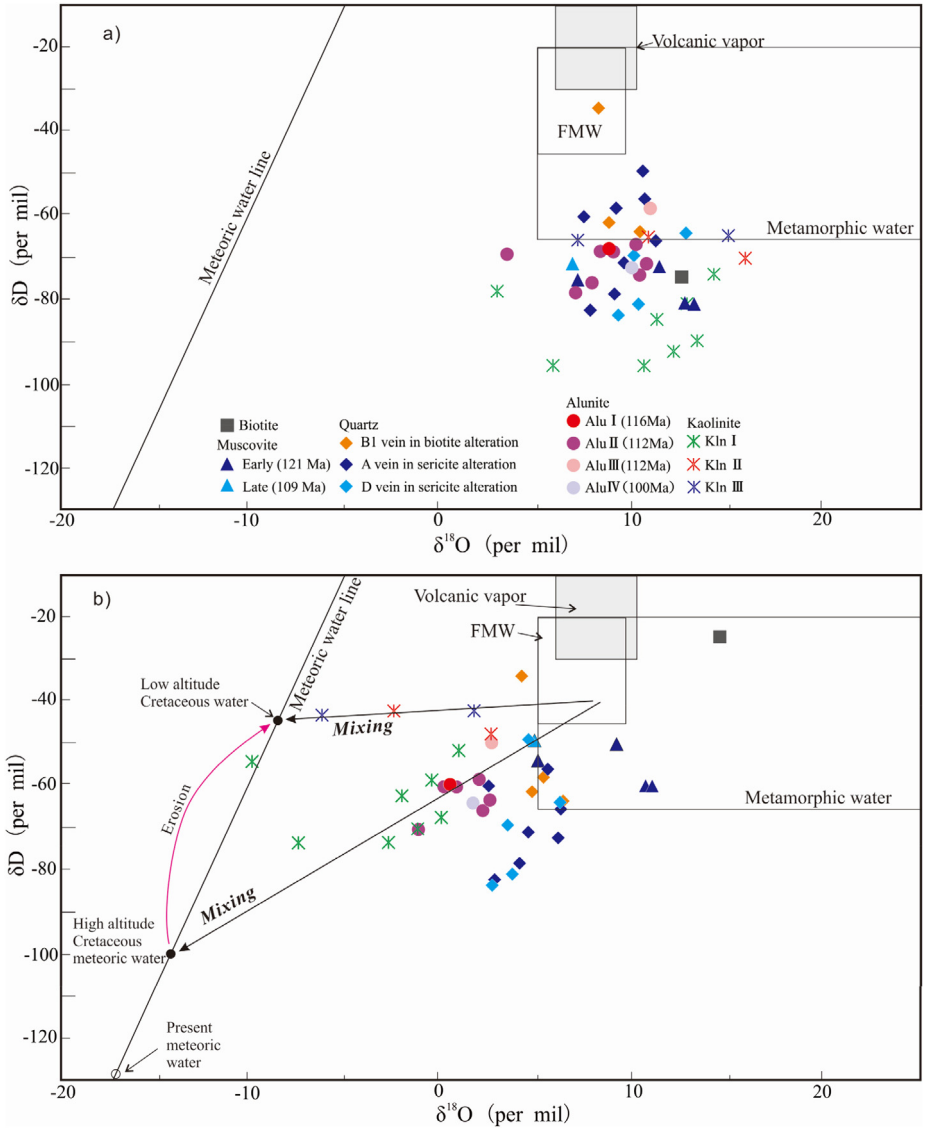

Fig. 5. a) Oxygen and hydrogen isotope compositions of minerals, and b) calculated hydrothermal fluid compositions. Quartz H data are from the fluid inclusions, FMW-felsic magmatic water (Taylor, 1992), volcanic vapor composition (Giggenbach, 1992), meteoric water line (Craig, 1961), metamorphic water (Taylor, 1974). Alu-alunite, Kln-kaolinite, Py-pyrite, Qz-quartz.

values of 7.1 and 15.1‰, and δD values of −66 and −65‰. Fluid compositions calculated for these two kaolinite yield $\delta^{18}O_{H2O}$ values of −6.0 and 2.0‰, and δD_{H2O} values of −43 and −41‰.

5.2. Sulfur isotopes

Sulfur isotope data from both bulk minerals and SIMS in situ spot analyses, and calculated fluid H_2S compositions equilibrium with pyrite, chalcopyrite, and enargite are listed in Table 2, calculation equations are given in Table 3.

Porphyry mineralization (Stages 1 and 2)

Three Stage 1 chalcopyrite and seven pyrite spots give SIMS $\delta^{34}S$ ranging from −2.6 to −0.7‰ for chalcopyrite, and from −5.8 to 0.9‰ for pyrite (Table. 2, Fig. 6a and 7). Fluid $\delta^{34}S_{H2S}$ compositions in equilibrium with pyrite and chalcopyrite, calculated using the pyrite-H_2S fractionation of Ohmoto and Rye (1979) and the chalcopyrite-H_2S fractionation of Li and Liu (2006), yield $\delta^{34}S_{H2S}$ values between −6.8 and −0.1‰ (mean = −2.5‰, n = 10) at a temperature of 350 °C. Five Stage 2 chalcopyrite grains yield SIMS $\delta^{34}S$ values between −8.7 and −3.0‰ (Table 2, Fig. 6b and 7). Calculated fluid composition $\delta^{34}S_{H2S}$ values are from −9.7 to −3.1 (mean = -5.6‰, n = 5) at a temperature of 350 °C.

5.2.1. Epithermal mineralization (Stages 4, 5, and 6)

Alunite I has a $\delta^{34}S$ value of 18.3‰, whereas pyrite in this alunite breccia returns a $\delta^{34}S$ value of −5.7‰. The alunite-pyrite pair yields an equilibrium temperature of 246 °C, based on the fractionation of Rye et al. (1992). Enargite in this alunite I breccia yields a $\delta^{34}S$ value −5.0‰.

The main epithermal mineralization stage alunite II-sulfide veins return alunite $\delta^{34}S$ values between 11 and 15.8‰, (mean = 13.3‰, n = 7), and yield varying Stage 3 pyrite $\delta^{34}S$ values from −32.2 to 5.4‰ (Table 2, Fig. 6 c-f). Two Stage 5 chalcopyrite give SIMS $\delta^{34}S$ values of −11.6 and −8.2‰ (Fig. 6e and f). Pyrite and chalcopyrite from two of these alunite II-sulfide veins (1604–171 and 1604–149) have different fluid $\delta^{34}S_{H2S}$ compositions (Table 2). Bulk mineral analysis of four Stage 6 enargite gives $\delta^{34}S$ values between −5 and −2.2‰ (Table. 2, Fig. 7b), which are distinct from chalcopyrite and pyrite $\delta^{34}S$ values. Fluid H_2S S isotope compositions in equilibrium with enargite is between −5.4 to −2.6‰ (Table 2), using fractionation of sphalerite-H_2S (Ohmoto and Rye, 1979) at a temperature of 250 °C, considering the similar structures between enargite and sphalerite (Hedenquist

Table 2
Mineral S isotope data and calculated fluid H_2S composition.

Samples	Description	S isotope values						
Porphyry mineralization Stage 1			Chalcopyrite		Pyrite			
			$\delta34S_{Ccp}$	$\delta34S_{H2S}$	$\delta34S_{Py}$	$\delta34S_{H2S}$		
3204–1066	Qz-Ccp-Py vein		**−2.6**	**−2.7**	**−4.4**	**−5.4**		
			−2.4	**−2.5**				
			−0.7	**−0.8**				
2404–903	Qz-Ccp-Bn-Py vein, Ccp-Bn replacing Py				**−1.6**	**−2.6**		
					−0.8	**−1.8**		
					−0.2	**−1.2**		
					0.9	**−0.1**		
2404–720	Disseminated Ccp-Bn repacing Py				**−5.8**	**−6.8**		
					−0.5	**−1.5**		
Porphyry mineralization Stage 2								
2404–720	Disseminated Ccp-Bn repacing Py		**−8.7**	**−9.7**				
			−6.7	**−7.7**				
			−3.2	**−4.2**				
2404–903	Qz-Ccp-Bn-Py vein, Ccp-Bn replacing Py		**−3.3**	**−3.4**				
			−3	**−3.1**				
Epithermal mineralization (Stage 4–6)			Stage 4 (pyrite)		Stage 5 (chalcopyrite)		Stage 6 (enargite)		
		$\delta34S_{Alu}$	$\delta34S_{Py}$	$\delta34S_{H2S}$	$\delta34S_{Ccp}$	$\delta34S_{H2S}$	$\delta34S_{Eng}$	$\delta34S_{H2S}$	$\Delta34S_{alu\text{-}py}$ (°C)
1604–429	Alu I breccia with Py and Eng	18.3	−5.7*	−7.2			−5	−5.4	246
0804–563	Alu II- Py vein	11.5	−2	−0.5					
0804–408	Alu II- Py- Eng vein	13.2	**−14.9***	**−16.4**					195
			−13.4*	**−14.9**					212
1604–375	Alu II- Py- Eng vein	15.7	−2.6	−4.1			−2.2	−2.6	
1604–171	Alu II- Py- Eng-Bn-Ccp vein	12.4	**−0.2,**	**−1.7**	**−11.6**	**−11.8**	−4.1	−4.5	
			3	**1.5**					
			5.4	**3.9**					
1604–149	Alu II- Py- Eng-Tnt-Dg-Ccp vein	13.2	**−9.5***	**−11**	**−8.2**	**−8.4**	−2.4	−2.8	266
			−10.7*	**−12.2**					247
			−27.1	**−28.6**					
			−32.2	**−33.7**					
1604–231	Alu II- Py- Eng-Tnt-Bn-Ccp vein	11	−0.7	−2.2					
4012–354	Alu II- Py-Ccp-Gn-Sph vein	15.8							
2412–511	Alu III in Qz-Py vein	6.6							
3212–206	Alu IV-Py	7.5	3	1.5					

Bold numbers are SIMS S isotope results. Pyrite-H_2S calculation from the fractionation of Ohmoto and Rye (1979); Chalcopyrite-H_2S calculation from the fractionation of Li and Liu (2006); Enargite-H2S are based on sphalerite-H_2S fractionation of Ohmoto and Rye (1979). *Pyrite $\delta^{34}S$ data used for $\Delta^{34}S_{alu\text{-}py}$ (°C) temperature calculation from the fractionation equation of Rye et al. (1992). Alu-alunite, Bn-bornite, Ccp-chalcopyrite, Dg-digenite, Eng-enargite, Gn-galena, Kln-kaolinite, Qz-quartz, Sph-sphalerite, Tnt-tennantite

et al., 2017).

One alunite III filling in quartz-pyrite vein gives a $\delta^{34}S$ value of 6.6‰, and pyrite from the quartz vein returns a $\delta^{34}S$ value of −3.4‰. Alunite IV has a $\delta^{34}S$ value of 7.5‰, and the pyrite in this alunite vein has $\delta^{34}S$ value of 3‰. The $\Delta^{34}S_{alunite\text{-}pyrite}$ is 4.3‰, which yields a geologically unreasonable fractionation temperature, suggesting alunite and pyrite are not in S isotopic equilibrium during formation of alunite IV.

6. Discussion

6.1. Origin of hydrothermal fluids

The composition of fluid in equilibrium with biotite, with a higher $\delta^{18}O$ value ($\delta^{18}O$ = 12.6‰) than that of felsic magmatic water, plots in the metamorphic water field (Fig. 5b). This biotite-bearing vein is hosted by biotite hornfels, formed by contact metamorphism of the

Table 3
Isotope Fractionation Equations and Factors.

Equation	References
Oxygen	
$103 \ln \alpha_{biotite\text{-}H2O} = 3.84 \times 10^6T^{-2}\text{-}8.76 \times 10^3T^{-1} + 2.46$	Zheng (1993b)
$103 \ln \alpha_{muscovite\text{-}H2O} = 2.39 \times 10^6T^{-2}\text{–}3.76$	Sheppard and Gilg (1996)
$103 \ln \alpha_{alunite(SO4)} = 3.09 \times 10^6T^{-2}\text{–}2.94$	Stoffregen et al. (1994)
$103 \ln \alpha_{kaolinite\text{-}H2O} = 2.76 \times 10^6T^{-2}\text{–}6.75$	Sheppard and Gilg (1996)
$103 \ln \alpha_{quartz\text{-}H2O} = 4.48 \times 10^6T^{-2}\text{–}4.77 \times 10^3T^{-1} + 1.71$	Zheng (1993a)
Hydrogen	
$103 \ln \alpha_{biotite\text{-}H2O} = \text{–}2.2 \times 10^6T^{-2}\text{–}7.7$	Suzuoki and Epstein (1976)
$103 \ln \alpha_{muscovite\text{-}H2O} = \text{–}20 \pm 5(350\ ^\circ C)$	Marumo et al. (1980)
$103 \ln \alpha_{alunite\text{-}H2O} = \text{-}6\ (250\ ^\circ C)$	Stoffregen et al. (1994)
$103 \ln \alpha_{kaolinite\text{-}H2O} = \text{–}2.2 \times 10^6T^{-2}\text{–}7.7$	Sheppard and Gilg (1996)
Sulfur	
$103 \ln \alpha_{alunite\text{-}pyrite} = 4.86 \times 10^6T^{-2} + 6$	Rye et al. (1992)
$103 \ln \alpha_{pyrite\text{-}H2S} = 0.4 \times 10^6T^{-2}$	Ohmoto and Rye (1979)
$103 \ln \alpha_{chalcopyrite\text{-}H2S} = 0.05 \times 10^6T^{-2}$	Li and Liu (2006)
$103 \ln \alpha_{sphalerite/enargite\text{-}H2S} = 0.1 \times 10^6T^{-2}$	Ohmoto and Rye (1979)

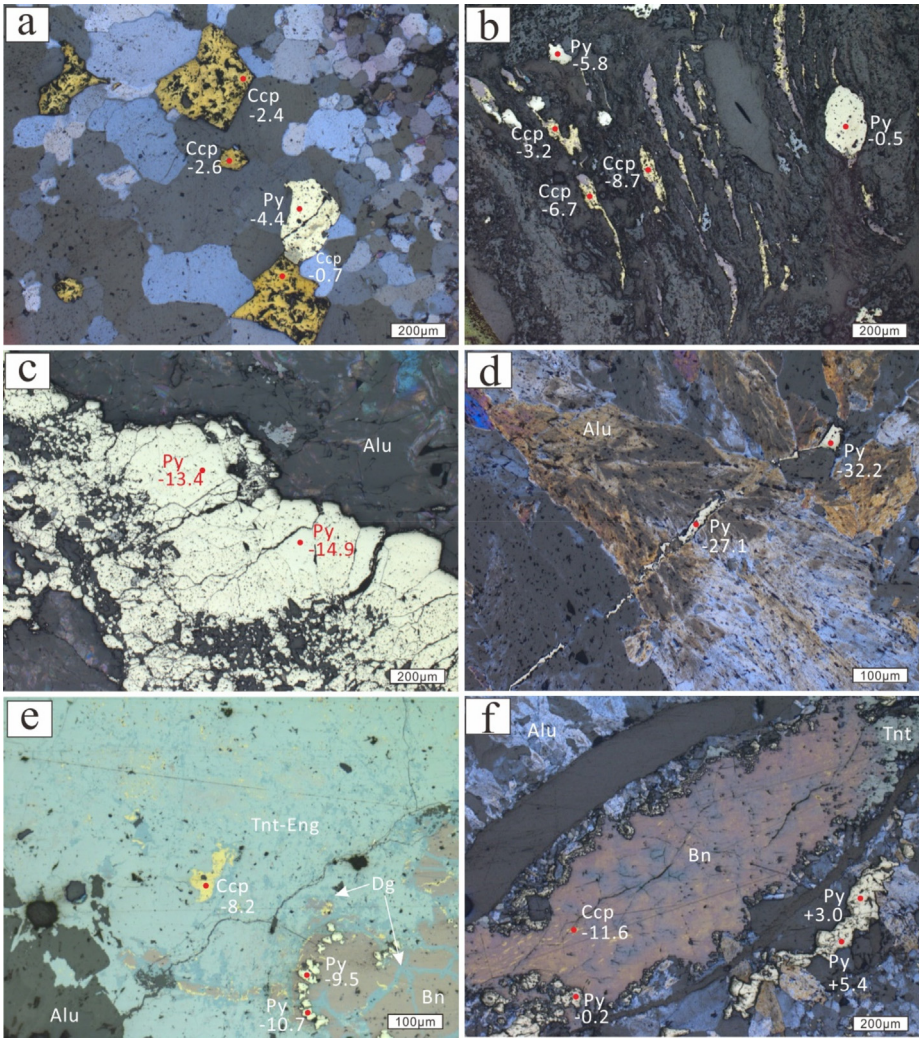

Fig. 6. SIMS sulfur isotope values (per mil) of sulfides. a)- Chalcopyrite and pyrite (Stage 1) in A-type quartz vein. b)-Disseminated bornite-chalcopyrite (Stage 2) replacing pyrite. c) and d)-Pyrite (Stage 4) in alunite vein. e)- Pyrite is replaced by bornite-chalcopyrite (Stage 5), and followed by enargite-tennantite (Stage 6) in alunite vein. f)-Pyrite replaced by bornite-chalcopyrite, and followed by tennantite. Alu-alunite, Bn-bornite, Ccp-chalcopyrite, Dg-digenite, Eng-enargite, Py-pyrite, Tnt-tennantite.

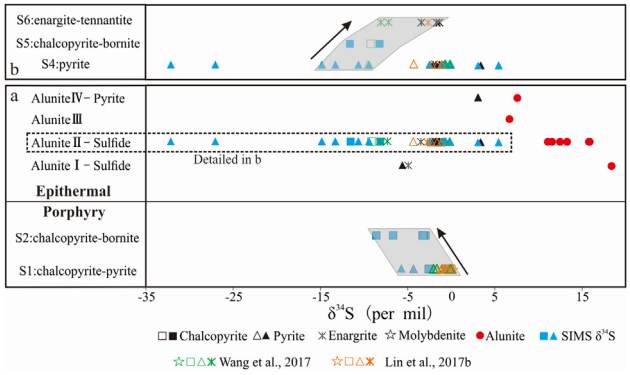

Fig. 7. Sulfur isotope ($\delta^{34}S$) composition of sulfide and sulfate minerals in porphyry and epithermal mineralizations at Tiegelongnan.

sedimentary protolith. The high $\delta^{18}O$ water composition during formation of the hydrothermal biotite may relate to the water from metamorphism of the sedimentary protolith without significant external water input. However, the number of hydrothermal biotite sample is inadequate, with only one obtained data, such that this conclusion shoud be cautiously regarded. On the other hand, the quartz data of B1 vein are mostly overlapping with quartz-muscovite-quartz fluid compositions (Fig. 5b), which suggest a magmatic water origin (see below).

The fluids in equilibrium with early muscovite (121 Ma) yield an average $\delta^{18}O_{H2O}$ of 8.9‰ and δD_{H2O} of −58‰ (n = 4), which is D-depeted compared to the felsic magmatic water field (Fig. 5b). Variable degrees of D depletion for sericite alteration are reported in porphyry deposits (Fig. 8). Harris and Golding (2002) interpreted the depletion of fluids δD for at Endeavour 26 North, Australia, as a result of vapor-brine fluids separation (or boiling), in which D-depleted brine fluid formed ore-related sericite alteration. Such a D-depleted brine fluid composition after phase separation is commonly observed during potassic (K-feldspar-biotite) alteration, and the δD fractionation between vapor and brine is estimated at ~20‰ (Hedenquist et al., 1998). Fluid boiling is interpreted from fluid inclusions petrology at Tiegelongnan (Yang et al., 2014; He et al., 2017), such that it could have caused the D-depletion during the quartz-muscovite-pyrite alteration. Alternatively, the D-depletion of magmatic water could result from the degassing of deep magma (Taylor, 1992; Shinohara and Hedenquist, 1997). Hedenquist et al. (1998) proposed D-depleted sericite alteration fluids due to degassing of magma, considering that sericite alteration in porphyry deposits tends to originate from younger hydrothermal fluids. The later D-depleted fluids are reported for the sericite alteration in several porphyry deposits, including Panguna, Papua New Guinea (Ford

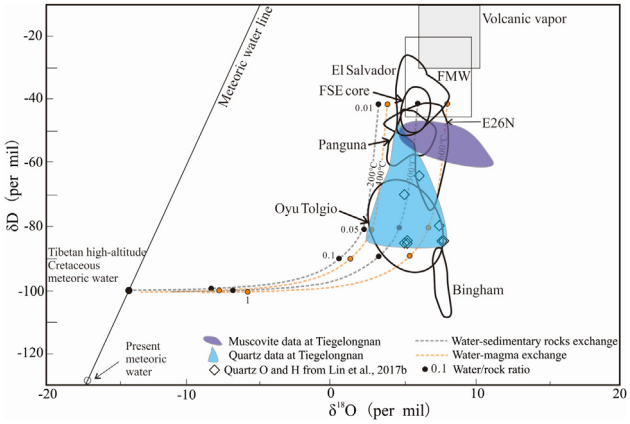

Fig. 8. Comparison of sericite (quartz-muscovite-pyrite) alteration fluid O and H isotope compositions between Tiegelongnan and other porphyry deposits, including data of Panguna, Papua New Guinea (Ford et al., 1977); Bingham, USA (Bowman et al., 1987); FSE, Philippines (Hedenquist et al., 1998); El Salvador, Chile (Watanabe and Hedenquist, 2001); Endeavour 26 North, Australia (Harris and Golding, 2002); Oyu Tolgoi, Mongolia Khashgerel et al., 2009). Calculations of water-rocks interaction using equations of Ohmoto and Rye, (1974), assuming an initial magma rock composition of $\delta^{18}O$ = 8‰ and δD = -40‰, and initial sediments rock composition of $\delta^{18}O$ = 16‰ and δD = -80‰. FMW-felsic magmatic water (Taylor, 1992), volcanic vapor composition (Giggenbach, 1992), meteoric water line (Craig, 1961).

et al., 1977), Bingham, USA (Bowman et al., 1987), Far South East, Philippines (Hedenquist et al., 1998), and Oyu Tolgoi, Mongolia (Khashgerel et al., 2009). The younger muscovite (109 Ma) fluid with $\delta^{18}O_{H2O}$ = 4.8 ‰and δD_{H2O} = −52‰, is similar with that of early muscovite (~121 Ma), suggesting they form from similar fluid compositions. Considering the indistinguishable spatial and petrological relationship between the two pulses of muscovite, the younger muscovite age might be a reset age that affected by andesite at ~110 Ma.

Fluid composition in equilibrium with A and D veins in the quartz-muscovite-pyrite alteration zone have average $\delta^{18}O_{H2O}$ values of 4.4‰, and 4.2‰, which are slightly lower than the estimated magmatic water composition ($\delta^{18}O$ = 8.9‰) for muscovite. Minor meteoric water mixing could slightly cause the decrease of fluid $\delta^{18}O$ values, such as the sericite alteration fluids compositions in El Salvador, Chile (Watanabe and Hedenquist, 2001), and Oyu Tolgoi, Mongolia (Khashgerel et al., 2009), as shown in Fig. 8. However, there is no evidence of meteoric water mixing for muscovite at Tiegelongnan (Fig. 8). Water-rock isotopic exchange would be another reason to cause the depletion of $\delta^{18}O$, with covariation δD values of hydroxyl-bearing minerals (Ohmoto and Rye, 1974).

Calculation of water and rocks isotopic exchange use equation of Ohmoto and Rye (1974) are assuming magma isotopic compositions of $\delta^{18}O$ = 9‰ and δD = −40‰, and sedimentary rocks with $\delta^{18}O$ of 16‰ and δD of −80‰ (Savin and Epstein, 1970). The high altitude Cretaceous meteoric water composition is estimated at $\delta^{18}O$ = −13.7‰ and δD = −100‰ (see below). Most of quartz and muscovite fluid compositions plot along the water-magma exchange paths between 400 °C and 600 °C, or along the water-sedimentary rock exchange paths between 200 °C and 300 °C with low water/rock ratios of less than ~0.05 (Fig. 8). The temperature range between 200 and 600 °C brackets quartz fluid inclusions homogenization temperatures of ~400 °C for B vein, 350–360 °C for A vein, and 230–320 °C for D vein (Yang et al., 2014; He et al., 2017). Water-rock isotope exchange does not cause lower of muscovite $\delta^{18}O$ values at low water/rocks ratios. Quartz $\delta^{18}O$ values, however, will decrease at low ratios of water-rock isotope exchange. The contrasting results between quartz and muscovite attribute to hydroxyl in muscovite, which could only slightly decrease δD without change of $\delta^{18}O$ values at low water/rock ratios. Some of the quartz fluid inclusions δD values from this study and those from Lin et al. (2017b) show lower fluid δD values than that for muscovite (Fig. 8). The lower δD values for fluid inclusions may result from the fractionation of H during quartz fluid inclusions thermal decrepitation and, possibly, by mechanical decrepitation (Faure, 2003).

Fluids in equilibrium with alunite plot along a mixing trend from felsic magmatic water towards the meteoric water line, suggesting that the formation of alunite veins results from mixing of magmatic and meteoric water. The mixing trend intersects the meteoric water line at a δD value of −100‰ (Fig. 5b), which represents the high altitude Cretaceous meteoric water composition in the Qiangtang area, that is higher than the present δD value of −128‰ (Zheng et al., 1982). Assuming a magmatic fluid composition with δD = −40‰, the ratios of magmatic to meteoric water during alunite formation range between 9:10 and 22:5, with an average ratio of 8:5 (n = 10). Type I kaolinite fluids also plot along the mixing trend towards the high altitude Cretacoueus meteoric water composition but with more scatter than that of alunite (Fig. 5b), suggesting they form from a similar fluid mixing processes to that of alunite. The average ratio of 8:5 equal to 62.5% magmatic water at Tiegelongnan is slightly lower than the estimated at over 75% magmatic water in other epithermal systems, such as Lepanto, Phillipines (Hedenquist et al., 1998), Pascua-Lama, Chile (Deyell et al., 2005), Summitville, USA (Bethke et al., 2005), and Oyu Tolgoi, Mongolia (Khashgerel et al., 2009), which suggests more intensive meteoric water admixture during formation of the Tiegelongnan epithermal system.

Water compositions in equilibrium with late Types II and III kaolinite that fills older alunite and quartz veins define a different mixing trend towards a δD value of about −45‰ along the meteoric water line (Fig. 5b). This meteoric water composition is comparable to the Cretaceous meteoric water composition in Gansu at the same latitude of 35°N (Amiot et al., 2011), but with at a lower altitude of 900 m. The low altitude meteoric water influx suggest types II and III kaolinite formed after the paleosurface subsidence of the Tibetan plateau. We converted the 55‰ δD difference to $\delta^{18}O$ difference of 6.9‰, using a global isotopic lapse rate of $\delta^{18}O$ = −0.28‰/100 m (Poage and Chamberlain, 2001), and estimate the 6.9‰ of $\delta^{18}O$ difference between high and low altitude meteoric water to represent ~2.5 km elevation change. If this elevation change was reliable, erosion should not be the only reason for elevation subsidence, because epithermal deposits commonly form at a depth of less than ~1.5 km (Simmons et al., 2005). Then, the ~2.5 km of erosion would have removed all the epithermal alteration and mineralization. Given the reservation of the epithermal mineralization at Tiegelongnan, the elevation decline most likely combines erosion and plateau subsidence.

6.2. Redox states evolution

Porphyry mineralization Stage 1 pyrite and chalcopyrite $\delta^{34}S$ values between −5.8 to 0.9‰ are comparable to $\delta^{34}S$ values of molybdenite, pyrite, and chalcopyrite between −2.5 and 0.8‰ obtained by Lin et al. (2017b) and Wang et al. (2017) (Fig. 7a). The Calculated average $\delta^{34}S_{H2S}$ = −2.5‰ for the early Stage 1 chalcopyrite-pyrite ± molybdenite mineralization is higher than the average $\delta^{34}S_{H2S}$ value of −5.6‰ during the Stage 2 chalcopyrite-bornite mineralization stage, which is most likely due to S isotopic fractionation with heavier sulfates at a higher oxidation state during the chalcopyrite-bornite mineralization stage. The oxidation state of porphyry-related hydrothermal fluids could be buffered through reaction with Fe-bearing minerals to increase the H_2S/SO_4^{2-} of the fluids (Giggenbach, 1997; Rye, 2005). Considering Stage 1 mineralization is associated with biotite alteration, whereas Stage 2 mineralization is related to quartz-muscovite-pyrite alteration, the weak buffer capability to reduce the high fO_2 porphyry hydrothermal fluids during quartz-muscovite-pyrite alteration is likely the reason for higher oxidation condition of Stage 2. Anhydrite is rare in the Tiegelongnan deposit, but one reported $\delta^{34}S$ value of 6.8‰, without associated sulfide S data to evaluate the S fractionation between sulfate

and sulfide (Lin et al., 2017b). Five gypsum in A and D veins returned $\delta^{34}S$ values between 0.3 and 1.5‰ (Lin et al., 2017b; Wang et al., 2017), which are close to the Stage 1 sulfides $\delta^{34}S$ values, suggesting they may have formed from dissolution and oxidizing of Stage 1 sulfides. Rare sulfate in the Tiegelongnan mineralization is perhaps due to dissolution by later meteoric water.

During the epithermal mineralization stages, seven of ten samples do not have alunite-pyrite S isotope equilibrium. Some Stage 4 pyrite samples have relatively high $\delta^{34}S$ values close to alunite $\delta^{34}S$ values, as in the sample 1604–171 (Table 2), perhaps because of rapid cooling during mixing with meteoric water that do not give sufficient time to reach S equilibrium. Retrograde isotope exchange between pyrite and later fluids could be another reason for the disequilibrium between alunite and pyrite pairs, since pyrite is commonly replaced by later Cu-sulfides with different $\delta^{34}S$ values (Fig. 6e and f). In addition, geochronology indicates multiple hydrothermal fluids overprinting events in the Tiegelongnan deposit (Yang et al., 2020).

The different $\delta^{34}S$ values between Stage 4 pyrite and later Stages 5 and 6 chalcopyrite and enargite were likely caused by a change of redox state. Several Stage 4 pyrite spots in S equilibrium with alunite have $\delta^{34}S$ values from −14.9 to −9.5‰. One epithermal vein-pyrite $\delta^{34}S$ value of −9.8‰ obtained by Wang et al. (2017) plots within this range (Fig. 7b). Wang et al. (2017) and Lin et al. (2017b) reported several higher epithermal vein pyrite $\delta^{34}S$ values between −4.6 and −0.4‰ (Fig. 7a), which are similar to some pyrite $\delta^{34}S$ values in disequilibrium with alunite. Unfortunately, there was no alunite analyzed in previous studies (Lin et al., 2017b; Wang et al., 2017), to discuss the S isotope fractionation between pyrite and alunite. Stage 5 chalcopyrite gives two $\delta^{34}S$ values of −11.6 and −8.2‰, which are similar to one chalcopyrite value of −9.8‰ from Wang et al. (2017) (Fig. 7b). Stage 6 enargite $\delta^{34}S$ values from −4.1 to −2.2‰ are identical to one data of −3.0‰ from Lin et al. (2017b), which are higher than two values of −7.5 and −8.5‰ from Wang et al. (2017). Generally, there is a trend of increasing $\delta^{34}S$ values from the Stage 4 to Stage 6 of sulfides (Fig. 7b). The associated fluid H_2S compositions also increase from Stage 4 of −16.4 to −11.0‰, to Stage 5 of −11.8 to −8.4‰, then to Stage 6 of −5.4 to −2.6‰ (Table 2), which suggests that the hydrothermal environment evolves towards more reducing conditions during the epithermal mineralization. This agrees with conclusions in high-sulfidation epithermal deposits that ore stage fluid is more reduced than pyrite stage, and Xso_4^{2-}/X_{H2S} were estimated between 1:3 and 1:5 for alunite-enargite (Arribas, 1995; Rye, 2005; Hedenquist et al., 2017), increasing to be 4:1 during alunite-pyrite stages (Hedenquist et al., 1993). Alunite-pyrite stage epithermal fluids are characterized by SO_2 and HCl vapor-rich fluids (Hedenquist et al., 1994), with high Xso_4^{2-}/X_{H2S} after the vapor condensing into water with the SO_2 disproportiontion reaction $4SO_2 + 4H_2O = 3H_2SO_4 + H_2S$ (Holland, 1965). In contast, epithermal ore-stage fluids are denser, and metals are mainly transported by reduced S-complex (Seward, 1973; Heinrich et al., 2004). The difference of fluid compositions between sulfide Stage 4 and that of Stage 5 and Stage 6 could be a reason for higher oxidation conditions during Stage 4. Continuous escape of vapor might result in more reducing conditions in younger stage of epithermal mineralization.

Replacement of hypogene by supergene alunite was recognized to decrease hypogene $\delta^{34}S$ of alunite to a lower value without affecting O and H isotopes, and it could reset argon isotopes in alunite geochronology (Watanabe and Hedenquist, 2001). The alunite IV $\delta^{34}S$ = 7.5‰ appears to be an example of this kind of mixed alunite, which may account for the young ^{40}Ar-^{39}Ar age of 100.6 ± 2.0 Ma.

7. Conclusions

Hydrogen and O stable isotopes suggest the muscovite alteration in the Tiegelongnan deposit is associated with magmatic water, while metamorphic water is likely involved with deep biotite alteration in hornfels. Several processes could affect the fluid compositions of sericite alteration, including vapor-brine separation, degassing of earlier magma, and water–rock isotopic exchange. Porphyry Stage 1 chalcopyrite-pyrite ± molybdenite mineralization has an average fluid $\delta^{34}S_{H2S}$ = -2.5‰, which is slightly higher than −5.6‰ of Stage 2 chalcopyrite-bornite stage, suggesting a higher oxidation state during the main chalcopyrite-bornite mineralization stage.

Alunite and Type I kalinite records mixing between magmatic and high altitude Cretaceous meteoric water with ~62.5% magmatic water. Late Types II and III barren kaolinite filling quartz veins and alunite veins defined a mixing line between magmatic and low altitude Cretaceous meteoric water, suggesting they may have formed after erosion and plateau subsidence. Several alunite-pyrite pairs do not in S isotope equilibrium are due to rapid cooling and retrograde S isotope exchange during later sulfides replacement. Pyrite, chalcopyrite, and enargite yield increasing fluids $\delta^{34}S_{H2S}$ values, suggesting they formed under different fluid compositions, and Cu mineralization stage fluids are more reduced than that of the alunite-pyrite stage.

Declaration of Competing Interest

The authors declare that they have no known competing financial interests or personal relationships that could have appeared to influence the work reported in this paper.

Acknowledgments

This work is jointed sponsored by the Public Science and Technology Research Funds Projects, National Key R&D Program of China, Deep Resources Exploration and Mining (No. 2018YFC0604106), and Natural Science Foundation Project (No. 41702080). The first author's doctoral study in Canada is sponsored by the China Scholarship Council. G. Beaudoin acknowledges NSERC for its long term support. We thank Evelyne Leduc (Queen's University) for help with bulk minerals H, O, and S isotope analyses, and Glenn Piercey (Memorial University of Newfoundland) for help with SIMS S isotope analyses. Constructive comments of Jeffrey Hedenquist, Mohammad Maanijou, and an anonymous referee significantly improved the manuscript.

References

Amiot, R., Wang, X., Zhou, Z., Wang, X., Buffetaut, E., Lecuyer, C., Ding, Z., Fluteau, F., Hibino, T., Kusuhashi, N., Mo, J., Suteethorn, V., Wang, Y., Xu, X., Zhang, F., 2011. Oxygen isotopes of East Asian dinosaurs reveal exceptionally cold Early Cretaceous climates. Proc. Natl. Acad. Sci. U.S.A. v. 108, 5179–5183.

Arribas Jr, A., 1995. Characteristics of high-sulfidation epithermal deposits, and their relation to magmatic fluid. Mineralogical Association of Canada Short Course 23, 419–454.

Bethke, P.M., Rye, R.O., Stoffregen, R.E., Vikre, P.G., 2005. Evolution of the magmatic-hydrothermal acid-sulfate system at Summitville, Colorado: integration of geological, stable-isotope, and fluid-inclusion evidence. Chem. Geol. 215, 281–315.

Bowman, J., Parry, W., Kropp, W., Kruer, S., 1987. Chemical and isotopic evolution of hydrothermal solutions at Bingham, Utah. Econ. Geol. 82, 395–428.

Chang, Z., Hedenquist, J.W., White, N.C., Cooke, D.R., Roach, M., Deyell, C.L., Garcia, J., Gemmell, J.B., McKnight, S., Cuison, A.L., 2011. Exploration tools for linked porphyry and epithermal deposits: Example from the Mankayan intrusion-centered Cu-Au district, Luzon, Philippines. Econ. Geol. 106, 1365–1398.

Clayton, R.N., Mayeda, T.K., 1963. The use of bromine pentafluoride in the extraction of oxygen from oxides and silicates for isotopic analysis. Geochim. Cosmochim. Acta v. 27, 43–52.

Craig, H., 1961. Isotopic variations in meteoric waters. Science 133, 1702–1703.

Deyell, C., Leonardson, R., Rye, R., Thompson, J., Bissig, T., Cooke, D., 2005. Alunite in the Pascua-Lama high-sulfidation deposit: constraints on alteration and ore deposition using stable isotope geochemistry. Econ. Geol. 100, 131–148.

Dilles, J.H., Solomon, G.C., Taylor, H.P., Einaudi, M.T., 1992. Oxygen and hydrogen isotope characteristics of hydrothermal alteration at the Ann-Mason porphyry copper deposit, Yerington, Nevada. Econ. Geol. 87, 44–63.

Ding, S., Chen, Y., Tang, J., Zheng, W., Lin, B., Yang, C., 2017. Petrogenesis and Tectonics of the Naruo Porphyry Cu (Au) Deposit Related Intrusion in the Duolong Area, Central Tibet. Acta Geol. Sin. (English Edition) 91, 581–601.

Fang, X., Tang, J., Song, Y., Yang, C., Ding, S., Wang, Y.-Y., Wang, Q., Sun, X.-G., Li, Y.-B., Wei, L.-J., 2015. Formation epoch of the South Tiegelong superlarge epithermal Cu (Au-Ag) deposit in Tibet and its geological implications. Acta Geosci. Sin. 36,

168–176.
Faure, K., 2003. δD values of fluid inclusion water in quartz and calcite ejecta from active geothermal systems: do values reflect those of original hydrothermal water? Econ. Geol. 98, 657–660.
Ford, J., Green, D., Hulston, J., Crick, I., Sheppard, S., 1977. Stable isotope studies on Bougainville and in Matupi Harbour, New Britain. Papua New Guinea: Geological Society, London, Special Publications 7, 162.
Giggenbach, W., 1992. Isotopic shifts in waters from geothermal and volcanic systems along convergent plate boundaries and their origin. Earth Planet. Sci. Lett. v. 113, 495–510.
Giggenbach, W., 1997, The origin and evolution of fluids in magmatic-hydrothermal systems: Geochemistry of hydrothermal ore deposits, v. 3, p. 737-796.
Gustafson, L.B., Hunt, J.P., 1975. The porphyry copper deposit at El Salvador, Chile. Econ. Geol. 70, 857–912.
Harris, A.C., Golding, S.D., 2002. New evidence of magmatic-fluid–related phyllic alteration: implications for the genesis of porphyry Cu deposits. Geology 30, 335–338.
He, W., Lin, B., Yang, H.-H., Fang, X., Song, Y.-X., Wei, S.-G., Hou, L., 2017. Fluid inclusion feature and its internal relationship with mineralization and epithermal alteration of the Tiegelongnan Cu-Au deposit. Acta Geosci. Sin. 38, 638–650.
Hedenquist, J.W., Aoki, M., Shinohara, H., 1994. Flux of volatiles and ore-forming metals from the magmatic-hydrothermal system of Satsuma Iwojima volcano. Geology 22, 585.
Hedenquist, J.W., Arribas, A.J., Reynolds, T.J., 1998. Evolution of an intrusion-centered hydrothermal system Far Southeast-Lepanto porphyry and epithermal Cu-Au Deposits, Philippine. Econ. Geol. 93, 373–404.
Hedenquist, J.W., Arribas, R., Aoki, M., 2017. Zonation of sulfate and sulfide minerals and isotopic composition in the Far Southeast porphyry and Lepanto epithermal Cu–Au Deposits, Philippines. Resour. Geol. 67, 174–196.
Hedenquist, J. W., Simmons S. F, Giggenbach W. F, and S, E. C., 1993, WhiteIsland, NewZealand, volcanic-hydrothermal system represents the geochemical environment of high-sulfidation Cu and Au ore deposition: Geology, v. 21, p. 4.
Hedenquist, J.W., Taran, Y.A., 2013. Modeling the formation of advanced argillic lithocaps: volcanic vapor condensation above porphyry intrusions. Econ. Geol. 108, 1523–1540.
Heinrich, C.A., Driesner, T., Stefánsson, A., Seward, T.M., 2004. Magmatic vapor contraction and the transport of gold from the porphyry environment to epithermal ore deposits. Geology 32, 761–764.
Holland, H.D., 1965. Some applications of thermochemical data to problems of ore deposits;[Part] 2, Mineral assemblages and the composition of ore forming fluids. Econ. Geol. 60, 1101–1166.
Khashgerel, B.-E., Rye, R.O., Kavalieris, I., Hayashi, K.-I., 2009. The sericitic to advanced argillic transition: stable isotope and mineralogical characteristics from the Hugo Dummett porphyry Cu-Au deposit, Oyu Tolgoi district, Mongolia. Econ. Geol. 104, 1087–1110.
Li, J.-X., Qin, K.-Z., Li, G.-M., Evans, N.J., Zhao, J.-X., Cao, M.-J., Huang, F., 2016a. The Nadun Cu–Au mineralization, central Tibet: root of a high sulfidation epithermal deposit. Ore Geol. Rev. 78, 371–387.
Li, J.X., Qin, K.Z., Li, G.M., Richards, J.P., Zhao, J.X., Cao, M.J., 2014. Geochronology, geochemistry, and zircon Hf isotopic compositions of Mesozoic intermediate–felsic intrusions in central Tibet: petrogenetic and tectonic implications. Lithos v. 198–199, 77–91.
Li, J.X., Qin, K.Z., Li, G.M., Xiao, B., Zhao, J.X., Cao, M.J., Chen, L., 2013. Petrogenesis of ore-bearing porphyries from the Duolong porphyry Cu–Au deposit, central Tibet: evidence from U-Pb geochronology, petrochemistry and Sr–Nd–Hf–O isotope characteristics. Lithos 160, 216–227.
Li, J.X., Qin, K.Z., Li, G.M., Xiao, B., Zhao, J.X., Chen, L., 2016b. Petrogenesis of Cretaceous igneous rocks from the Duolong porphyry Cu–Au deposit, central Tibet: evidence from zircon U-Pb geochronology, petrochemistry and Sr–Nd–Pb–Hf isotope characteristics. Geol. J. 51, 285–307.
Li, X.K., Li, C., Sun, Z.M., Wang, M., 2017. Origin and tectonic setting of the giant Duolong Cu–Au deposit, South Qiangtang Terrane, Tibet: evidence from geochronology and geochemistry of Early Cretaceous intrusive rocks. Ore Geol. Rev. 80, 61–78.
Li, Y., Liu, J., 2006. Calculation of sulfur isotope fractionation in sulfides. Geochim. Cosmochim. Acta 70, 1789–1795.
Lin, B., Chen, Y., Tang, J., Wang, Q., Song, Y., Yang, C., Wang, W., He, W., Zhang, L., 2017a. 40Ar/39Ar and Rb-Sr Ages of the Tiegelongnan Porphyry Cu-(Au) Deposit in the Bangong Co-Nujiang Metallogenic Belt of Tibet. Implication for Generation of Super-Large Deposit: Acta Geologica Sinica (English Edition), China, pp. 602–616.
Lin, B., Tang, J., Chen, Y., Baker, M., Song, Y., Yang, H., Wang, Q., He, W., Liu, Z., 2018. Geology and geochronology of Naruo large porphyry-breccia Cu deposit in the Duolong district, Tibet. Gondwana Res. 66, 168–182.
Lin, B., Tang, J.X., Chen, Y.C., Song, Y., Hall, G., Wang, Q., Yang, C., Fang, X., Duan, J.l., and Yang, H.H., 2017b, Geochronology and Genesis of the Tiegelongnan Porphyry Cu (Au) Deposit in Tibet: Evidence from U–Pb, Re–Os Dating and Hf, S, and H–O Isotopes: Resource Geology, v. 67, pp. 1-21.
Marumo, K., Nagasawa, K., Kuroda, Y., 1980. Mineralogy and hydrogen isotope geochemistry of clay minerals in the Ohnuma geothermal area, northeastern Japan. Earth Planet. Sci. Lett. 47, 255–262.
O'Neil, J.R., Taylor, H.P., 1969. Oxygen isotope equilibrium between muscovite and water. J. Geophys. Res. 74, 6012–6022.
Ohmoto, H., Rye, R., 1979. In: Isotopes of sulfur and carbon. Geochemistry of Hydrothermal Ore Deposits. John Wiley & Sons Inc., New York, pp. 509–567.
Ohmoto, H., Rye, R.O., 1974. Hydrogen and oxygen isotopic compositions of fluid inclusions in the Kuroko deposits, Japan. Econ. Geol. 69, 947–953.
Orovan, E.A., Cooke, D.R., Harris, A.C., Ackerman, B., Lawlis, E., 2018. Geology and isotope geochemistry of the Wainaulo Cu-Au porphyry deposit, Namosi district, Fiji. Econ. Geol. 113, 133–161.
Poage, M.A., Chamberlain, C.P., 2001. Empirical relationships between elevation and the stable isotope composition of precipitation and surface waters: considerations for studies of paleoelevation change. Am. J. Sci. 301, 1–15.
Rye, R.O., 1993. The evolution of magmatic fluids in the epithermal environment; the stable isotope perspective. Econ. Geol. 88, 733–752.
Rye, R.O., 2005. A review of the stable-isotope geochemistry of sulfate minerals in selected igneous environments and related hydrothermal systems. Chem. Geol. 215, 5–36.
Rye, R.O., Bethke, P.M., Wasserman, M.D., 1992. The stable isotope geochemistry of acid sulfate alteration. Econ. Geol. 87, 225–262.
Savin, S.M., Epstein, S., 1970. The oyxgen and hydrogen isotope geochemistry of ocean sediments and shales. Geochim. Cosmochim. Acta 34, 43–63.
Seedorff, E., Dilles, J., Proffett, J., Einaudi, M., Zurcher, L., Stavast, W., Johnson, D., and Barton, M., 2005, Porphyry deposits: characteristics and origin of hypogene features: Economic Geology 100th anniversary volume, v. 29, p. 251-298.
Seward, T.M., 1973. Thio complexes of gold and the transport of gold in hydrothermal ore solutions. Geochim. Cosmochim. Acta 37, 379–399.
Sheppard, S., Gilg, H., 1996. Stable isotope geochemistry of clay minerals. Clay Miner. 31, 1–24.
Sheppard, S.M., Taylor, H., 1974. Hydrogen and oxygen isotope evidence for the origins of water in the Boulder batholith and the Butte ore deposits, Montana. Econ. Geol. 69, 926–946.
Shinohara, H., Hedenquist, J., 1997. Constraints on magma degassing beneath the Far Southeast porphyry Cu–Au deposit, Philippines. J. Petrol. 38, 1741–1752.
Sillitoe, R.H., 2005. Supergene oxidized and enriched porphyry copper and related deposits. Econ. Geol. 100, 723–768.
Simmons, S. F., White, N. C., and John, D. A., 2005, Geological characteristics of epithermal precious and base metal deposits: Economic Geology 100th anniversary volume, v. 29, pp. 485-522.
Song, Y., Yang, C., Wei, S., Yang, H., Fang, X., Lu, H., 2018. Tectonic Control, Reconstruction and Preservation of the Tiegelongnan Porphyry and Epithermal Overprinting Cu (Au) Deposit, Central Tibet, China. Minerals 8, 398–415.
Stoffregen, R.E., 1987. Genesis of acid-sulfate alteration and Au-Cu-Ag mineralization at Summitville, Colorado. Econ. Geol. 82, 1575–1591.
Stoffregen, R.E., Rye, R.O., Wasserman, M.D., 1994. Experimental studies of alunite: I. 18O–16O and DH fractionation factors between alunite and water at 250–450 C. Geochim. Cosmochim. Acta v. 58, 903–916.
Sun, J., Mao, J., Beaudoin, G., Duan, X., Yao, F., Ouyang, H., Wu, Y., Li, Y., Meng, X., 2017. Geochronology and geochemistry of porphyritic intrusions in the Duolong porphyry and epithermal Cu-Au district, central Tibet: implications for the genesis and exploration of porphyry copper deposits. Ore Geol. Rev. 80, 1004–1019.
Suzuoki, T., Epstein, S., 1976. Hydrogen isotope fractionation between OH-bearing minerals and water. Geochim. Cosmochim. Acta 40, 1229–1240.
Tang, J.-X., Wang, Q., Yang, H.-H., Gao, X., Zhang, Z.-B., Zou, B., 2017. Mineralization, exploration and resource potential of porphyry-skarn-epithermal copper polymetallic deposits in Tibet. Acta Geosci. Sin. 38, 571–613.
Tang, J., Sun, X., Ding, S., Wang, Q., Wang, Y., Yang, C., Chen, H., Li, Y., Li, Y., Wei, L., 2014. Discovery of the epithermal deposit of Cu (Au-Ag) in the Duolong ore concentrating area, Tibet. Acta Geosci. Sin. 35, 6–10.
Taylor, H.P, 1974. The application of oxygen and hydrogen isotope studies to problems of hydrothermal alteration and ore deposition. Econ. Geol. 69 (6), 843–883.
Taylor, B.E., 1992. Degassing of H_2O from Rhyolite Magma during Eruption and Shallow Intrusion, and the Isotopic Composition of Magmatic Water in Hydrothermal Systems (Japan-US Seminar on Magmatic Contributions to Hydrothermal Systems). Japan Geol. Survey Report.
Wang, q., Juxing, T., Xiang, F., Bin, L., Yang, S., Yiyun, W., Huanhuan, Y., Chao, Y., Yanbo, L., and Lujie, W., 2015, Petrogenetic setting of andsites in Rongna ore block, Tiegelong Cu (Au–Ag) deposit, Duolong ore concentration area, Tibet: evidence from zircon U–Pb LA–ICP–MS dating and petrogeochemistry of andsites: Geology in China, v. 42, p. 1324-1336.
Wang, Y.-Y., Tang, J.-X., Song, Y., Lin, B., Yang, C., Qin, W., Gao, K., Ding, S., 2017. Geochemical Characteristics of Sulfur and Lead Isotopes from the Superlarge Tiegelongnan Copper (Gold-silver) Deposit, Tibet. Acta Geosci. Sin. 38, 627–637.
Watanabe, Y., Hedenquist, J.W., 2001. Mineralogic and stable isotope zonation at the surface over the El Salvador porphyry copper deposit, Chile. Econ. Geol. 96, 1775–1797.
Yang, Chao, Tang, Juxing, Beaudoin, Georges, Song, Yang, Lin, Bin, Wang, Qin, Fang, Xiang, 2020. Geology and geochronology of the Tiegelongnan porphyry-epithermal Cu (Au) deposit, Tibet, China: formation, exhumation and preservation history. Ore Geol. Rev. 123, 103575.
Yang, C., Tang, J., Wang, Y., Yang, H., Wang, Q., Sun, X., Feng, J., Yin, X., Ding, S., Fang, X., 2014. Fluid and geological characteristics researches of Southern Tiegelong epithermal porphyry Cu-Au deposit in Tibet. Mineral Deposits 33, 1287–1305.
Yanites, B.J., Kesler, S.E., 2015. A climate signal in exhumation patterns revealed by porphyry copper deposits. Nat. Geosci. 8, 462–466.
Zhang, X.-N., Li, G.-M., Qin, K.-Z., Lehmann, B., Li, J.-X., Zhao, J.-X., Cao, M.-J., Zou, X.-Y., 2018. Petrogenesis and tectonic setting of Early Cretaceous granodioritic porphyry from the giant Rongna porphyry Cu deposit, central Tibet. J. Asian Earth Sci. 161, 74–92.
Zheng, S., Zhang, Z., Ni, B., Hou, F., Shen, M., 1982. Hydrogen and oxygen isotopic studies of thermal waters in Xizang. Acta Scientiarum Naturalium Universitatis Pekinensis 1, 99–106.
Zheng, Y.-F., 1993a. Calculation of oxygen isotope fractionation in anhydrous silicate minerals. Geochim. Cosmochim. Acta 57, 1079–1091.
Zheng, Y.-F., 1993b. Calculation of oxygen isotope fractionation in hydroxyl-bearing silicates. Earth Planet. Sci. Lett. 120, 247–263.
Zhu, D.-C., Li, S.-M., Cawood, P.A., Wang, Q., Zhao, Z.-D., Liu, S.-A., Wang, L.-Q., 2016. Assembly of the Lhasa and Qiangtang terranes in central Tibet by divergent double subduction. Lithos 245, 7–17.